

ARTICLE

Received 26 Oct 2014 | Accepted 8 Jul 2015 | Published 14 Aug 2015

DOI: 10.1038/ncomms9014

OPEN

Visualizing nanoscale 3D compositional fluctuation of lithium in advanced lithium-ion battery cathodes

A. Devaraj¹, M. Gu¹, R. Colby^{1,†}, P. Yan¹, C.M. Wang¹, J.M. Zheng², J. Xiao², A. Genc³, J.G. Zhang², I. Belharouak⁴, D. Wang⁵, K. Amine⁵ & S. Thevuthasan^{1,4}

The distribution of cations in Li-ion battery cathodes as a function of cycling is a pivotal characteristic of battery performance. The transition metal cation distribution has been shown to affect cathode performance; however, Li is notoriously challenging to characterize with typical imaging techniques. Here laser-assisted atom probe tomography (APT) is used to map the three-dimensional distribution of Li at a sub-nanometre spatial resolution and correlate it with the distribution of the transition metal cations (*M*) and the oxygen. As-fabricated layered $\text{Li}_{1.2}\text{Ni}_{0.2}\text{Mn}_{0.6}\text{O}_2$ is shown to have Li-rich Li_2MO_3 phase regions and Li-depleted $\text{Li}(\text{Ni}_{0.5}\text{Mn}_{0.5})\text{O}_2$ regions. Cycled material has an overall loss of Li in addition to Ni-, Mn- and Li-rich regions. Spinel $\text{LiNi}_{0.5}\text{Mn}_{1.5}\text{O}_4$ is shown to have a uniform distribution of all cations. APT results were compared to energy dispersive spectroscopy mapping with a scanning transmission electron microscope to confirm the transition metal cation distribution.

¹Environmental and Molecular Sciences Laboratory, Pacific Northwest National Laboratory, Richland, Washington 99354, USA. ²Energy and Environmental Directorate, Pacific Northwest National Laboratory, Richland, Washington 99354, USA. ³FEI Company, 5350 NE Dawson Creek Dr., Hillsboro, Oregon 97124, USA. ⁴Qatar Environment and Energy Research Institute, Qatar Foundation, PO box 5825, Doha, Qatar. ⁵Chemical Sciences and Engineering Division, Argonne National Laboratory, Argonne, Illinois 60439, USA. † Present address: ExxonMobil Research and Engineering Company, Annandale, New Jersey 08801, USA. Correspondence and requests for materials should be addressed to A.D. (email: arun.devaraj@pnnl.gov).

The portable consumer electronics revolution has driven the development of Li-ion batteries for efficient energy storage over the last decade^{1,2}. Currently, there is also a strong interest in developing cost-effective, rapidly recharging Li-ion batteries suitable for long range electric vehicles³. As cathodes constitute a substantial portion of the volume and cost of a battery significant effort has been focused on the development of next-generation cathode materials^{4,5}. Designing materials that can retain structural integrity after repeated cycling is a substantial challenge⁴. Fast ionic transport during electrochemical cycling of a material depends critically on the initial structure and crystal stability. The presence and stability of channels for fast Li-ion diffusion in cathode materials is an important design criterion for developing next-generation cathode materials for Li-ion batteries with higher capacity and long-term energy storage performance. Understanding nanoscale distribution of all of the elements that makeup Li-ion battery cathodes—especially Li ions—as a function of different synthesis procedures and extents of electrochemical cycling is a critical step towards developing new materials.

Li-rich layered cathode materials with the general formulae $\text{Li}[\text{Li}_{1/2-2x/3}\text{Ni}_x\text{Mn}_{2/3-x/3}]\text{O}_2$ where $0 < x < 1/3$ and more specifically, $\text{Li}_{1.2}\text{Ni}_{0.2}\text{Mn}_{0.6}\text{O}_2$ —have been demonstrated with capacities $> 250 \text{ mAh g}^{-1}$; significantly higher than the 140 mAh g^{-1} capacity of the best LiCoO_2 cathodes, used widely in consumer electronics^{6–9}. Structurally layered $\text{Li}_{1.2}\text{Ni}_{0.2}\text{Mn}_{0.6}\text{O}_2$ is considered to be a phase mixture of the trigonal LiMO_2 (R-3m) and monoclinic Li_2MO_3 (C2/m) phases ($M = \text{Ni, Mn}$). Both of these structures can be represented as repeating layers of transition metal ions, O and Li. Recently, compositional segregation of Ni to surfaces and grain boundaries within some particles and partitioning of Mn away from Ni-rich regions in layered $\text{Li}_{1.2}\text{Ni}_{0.2}\text{Mn}_{0.6}\text{O}_2$ has been shown by energy dispersive spectroscopy (EDS) tomography^{10–12}. By comparison of high-angle annular dark-field scanning transmission electron microscopy (HAADF-STEM) images to multislice simulations, the Ni-rich regions were shown to be consistent with an R-3m phase and the Ni-deficient regions a C2/m phase¹². Electron energy-loss spectroscopy (EELS) analysis has indicated a 7:9 Ni:Mn ratio (0.77) in the Ni-rich regions, best matching $\text{Li}(\text{Ni}_{0.5}\text{Mn}_{0.5})\text{O}_2$, and a 5:42 Ni:Mn ratio (0.12) in the Ni-deficient regions, best matching Li_2MnO_3 (ref. 12). X-ray diffraction from as-prepared $\text{Li}_{1.2}\text{Ni}_{0.2}\text{Mn}_{0.6}\text{O}_2$ predominantly matched an R-3m structure, with the exception of three peaks between 20 and 25° matching the C2/m structure^{8,13,14}. However, no detailed information was found on the distribution of Li, or of its correlation to other elements in the lattice, within the published literature.

Under battery charge–discharge cycling, layered $\text{Li}_{1.2}\text{Ni}_{0.2}\text{Mn}_{0.6}\text{O}_2$ cathodes were observed to develop a thin surface reconstruction layer, featuring structural transformation, Mn and Ni enrichment, oxygen vacancy formation and Li depletion^{15–17}. Due to the structural and chemical change of the thin surface layer, it is believed to be a likely main contributor to voltage fading¹⁸. Furthermore, it has been proven that the surface layer continues to grow in thickness during continuous cycling^{15,19}. EDS analysis of cycled layered $\text{Li}_{1.2}\text{Ni}_{0.2}\text{Mn}_{0.6}\text{O}_2$ has indicated composition variations even within the thin surface reconstruction layer¹⁵. To understand the structural degradation mechanism and seek a means to suppress the surface reconstruction, requires monitoring the evolution of all elements quantitatively at different states of cycling. However, despite substantial characterization efforts in previous studies, quantifying lithium depletion and subtle changes in oxygen concentration in the surface layer have been proven to be elusively challenging.

High-voltage spinel $\text{LiNi}_{0.5}\text{Mn}_{1.5}\text{O}_4$, is considered one of the most promising candidates for hybrid electric vehicle batteries^{2,20,21}. Stoichiometric $\text{LiNi}_{0.5}\text{Mn}_{1.5}\text{O}_4$ is known to have a spinel structure with ordered P4₃2 or disordered Fd3m, depending on the post-synthesis annealing temperature^{22–24}. This order–disorder phase transformation is expected to occur during higher temperature annealing as a result of generation or elimination of oxygen vacancies, by affecting the presence of Mn^{3+} in the lattice^{23,24}. The disordered phase of $\text{LiNi}_{0.5}\text{Mn}_{1.5}\text{O}_4$ is shown to have better electrochemical performance than the ordered spinel, owing to its higher electronic conductivity in the presence of increased disordered phase and/or Mn^{3+} concentration^{22,24–27}.

The common obstacle to using these materials is capacity and voltage fading, believed to be closely related to a gradual structural evolution, governed by the spatial distribution of Li ions and their correlation with other ions in the lattice. Therefore, one of the great challenges facing the development of these high-voltage cathode materials for Li-ion batteries is to locate the spatial distribution of ions with sub-nanometre-scale spatial resolution. Aberration-corrected scanning and conventional transmission electron microscopy (S/TEM)^{28–31} and soft X-ray imaging/spectroscopy³² have been used to spatially map the transition metal cations within Li-ion battery cathodes, but these techniques do not have sufficient sensitivity to map Li at sub-nanometre scales, especially in three-dimensional (3D). Atom probe tomography (APT) is uniquely capable of providing quantitative 3D, sub-nanometre-scale compositional characterization of oxides and composites^{33–38}, with sensitivity for the Li, the O, and the transition metal cations^{39–50} in a Li-ion cathode material. While $\text{Li}_{1.2}\text{Ni}_{0.2}\text{Mn}_{0.6}\text{O}_2$ is expected to be a two-phase mixture, $\text{LiNi}_{0.5}\text{Mn}_{1.5}\text{O}_4$ is expected to have a uniform cation distribution, providing a baseline evaluation of the ability of APT in unambiguously analysing the Li distribution in Li-ion battery cathode materials.

With this goal in mind, we provide here the first evidence for achieving unambiguous 3D sub-nanometre-scale spatially resolved mapping of Li, Ni, Mn and O in two categories of the advanced Li-ion battery cathode materials: layered- $\text{Li}[\text{Li}_{0.2}\text{Ni}_{0.2}\text{Mn}_{0.6}]\text{O}_2$ and spinel $\text{LiNi}_{0.5}\text{Mn}_{1.5}\text{O}_4$, using APT. APT results from as-fabricated and cycled layered- $\text{Li}[\text{Li}_{0.2}\text{Ni}_{0.2}\text{Mn}_{0.6}]\text{O}_2$ are compared with obtain insights towards mechanisms for cycling dependent capacity loss.

Results

Element distribution in as-fabricated $\text{Li}_{1.2}\text{Ni}_{0.2}\text{Mn}_{0.6}\text{O}_2$. Before APT analysis, the layered- $\text{Li}[\text{Li}_{0.2}\text{Ni}_{0.2}\text{Mn}_{0.6}]\text{O}_2$ and spinel $\text{LiNi}_{0.5}\text{Mn}_{1.5}\text{O}_4$ particles—henceforth, layered-LNMO and spinel-LNMO—were analysed using STEM imaging and EDS mapping. An annular dark-field STEM image and EDS maps of a typical layered-LNMO particle are shown in Fig. 1a–e providing a clear evidence of non-uniform distribution of Ni and Mn within a nanoparticle. A layered-LNMO nanoparticle was subsequently analysed with APT using 20-pJ laser pulse energy to image and quantify Li, Ni, Mn and O distributions. In the atom-probe mass-to-charge spectra of layered-LNMO, elemental peaks of Li^{1+} , Ni^{1+} , Ni^{2+} , Mn^{1+} , Mn^{2+} and O^{1+} are visible, in addition to molecular species peaks for O_2^+ , MnO^{1+} , MnO_2^+ , MnO_3^+ , MnO_4^+ , Mn_2O_2^+ , Mn_2O_3^+ , Mn_2O_4^+ , Mn_2O_5^+ , Mn_2O_6^+ , NiO^{1+} , NiO_2^+ , NiO_3^+ , NiO_4^+ , Ni_2O_2^+ , Ni_2O_3^+ , MnNiO_2^+ , MnNiO_3^+ and MnNiO_4^+ (Supplementary Fig. 1). Of the total ion counts, 80.12% corresponded to elemental evaporation of Li, Ni, Mn and O. Out of all the molecular species evaporated, O_2 , MnO, NiO, MnO_2 and MnO_3 combined

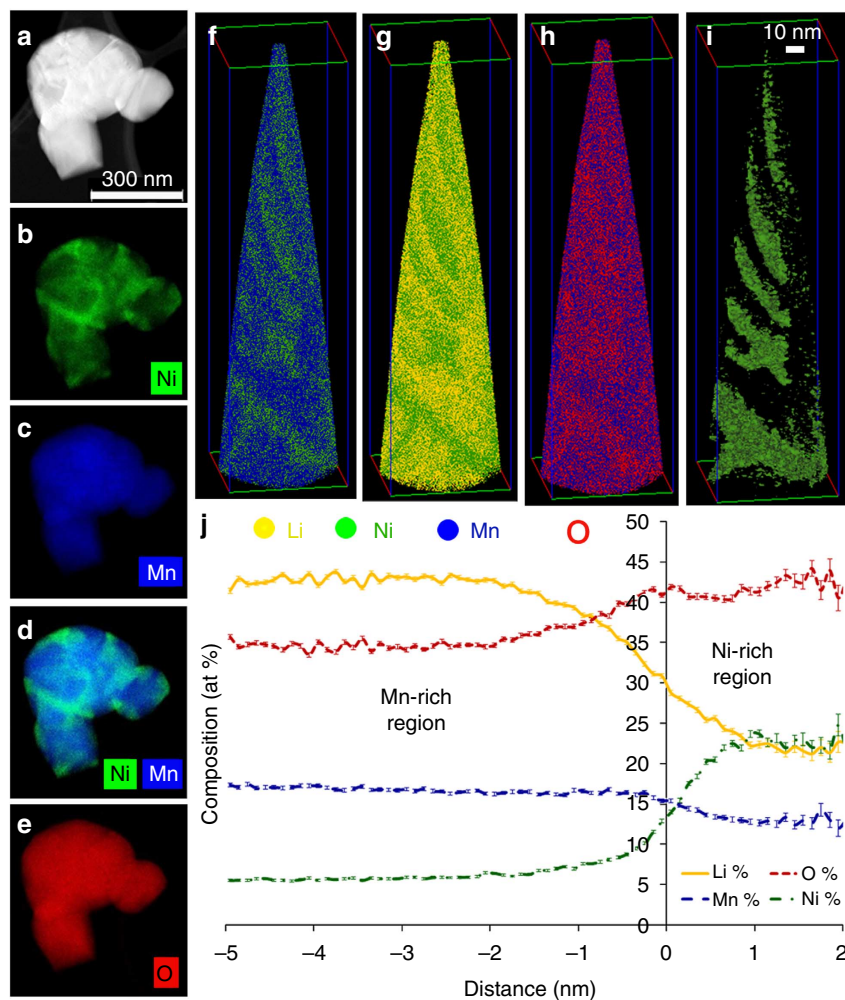


Figure 1 | Comparison of TEM EDS tomography with APT results of layered-LNMO. (a) STEM image and EDS maps of (b) Ni (green) (c) Mn (blue) (d) Ni and Mn composite map (e) O (red). Two element composite maps of the APT reconstructions are shown from f to h where each dot correspond to an atom in the reconstruction. (f) Mn (blue) and Ni (green) ion distribution (g) Li (yellow) and Ni (green) ion distribution and (h) O (red) and Mn (blue) ion distribution. (i) 13 at % Ni isocomposition surface highlighting the Ni-rich regions in the reconstruction (j) Proximity histogram⁵¹ obtained across the 13 at% Ni isocomposition surface showing concentration partitioning between Ni-rich and Mn-rich regions.

constituted 18.37% of the total ion counts. All remaining complex ions corresponded to only 1.51% of the total ion counts. Such complex molecular species evaporation is commonly observed during laser-assisted APT analysis of other metal oxides, such as for MgO (ref. 33). The measured concentrations from the APT reconstruction were 41.61 ± 0.03 at% Li, 6.13 ± 0.01 at% Ni, 16.60 ± 0.02 at% Mn, and 35.66 ± 0.03 at% O. The expected atomic concentrations are 30 at% Li, 5 at% Ni, 15 at% Mn, and 50 at% O.

Oxygen is known to be deficient during laser-assisted APT analysis of oxides except at extremely low laser energies³³. To verify the accuracy of the APT quantification, the measured concentrations of Li, Mn and Ni were renormalized independently of O and compared with the expected composition. In stoichiometric $\text{Li}_{1.2}\text{Ni}_{0.2}\text{Mn}_{0.6}\text{O}_2$, the Li fraction of the total cations, $\text{Li}/(\text{Li} + \text{Mn} + \text{Ni})$, should be 0.6; Mn, 0.3; and Ni, 0.1. The measured cation fractions were 0.647, 0.258 and 0.095, respectively. The concentration these specimens will be a function of the volume fraction of Ni-rich and Mn-rich regions sampled within the reconstruction, which may account for the minor variation from the expected stoichiometry. The APT reconstruction from layered-LNMO is shown in Fig. 1f–i). The non-uniform spatial distribution of Mn (blue) and Ni (green)

ions shown in Fig. 1f is comparable to EDS maps shown in Fig. 1b–d). The ion map showing Li (yellow) with Ni (green) highlights the similarity of the spatial distribution of Li and Mn. Both Li and Mn segregate away from regions of Ni enrichment (Fig. 1g). The O (red) and Mn (blue) ion map shows O segregating to regions with Ni enrichment (Fig. 1h). A 13 at% Ni isocomposition surface image, shown in Fig. 1i, highlights regions enriched in Ni distributed throughout the reconstructed volume. The compositional partitioning across the Ni- and Mn-rich regions was quantified using a proximity histogram calculated perpendicular to the 13 at% Ni isocomposition surface⁵¹ (Fig. 1j). From the steady-state regions on either side of the interface in proximity histogram, the concentration of Ni-rich region was estimated to be 21.92 ± 0.83 at% Li, 12.89 ± 0.67 at% Mn, 22.65 ± 0.84 at% Ni and 42.53 ± 0.99 at% O and the Mn-rich regions had a concentration of 42.94 ± 0.29 at% Li, 16.91 ± 0.22 at% Mn, 5.69 ± 0.14 at% Ni and 34.36 ± 0.28 at% O. The Ni:Mn ratios in the Ni-rich region and Mn-rich region correspond to 1.76 and 0.34, respectively. These Ni:Mn ratios are considerably higher than those previously obtained from Mn- or Ni-rich regions with STEM-EELS measurements, but two-dimensional (2D) STEM-based maps are measured in projection and thus an average of the

composition through the thickness of the LMNO particle. The truly 3D measurements made by APT would therefore be expected to yield a higher maximum Ni:Mn ratio in 3D Ni- or Mn-rich regions.

To quantify the extent of phase separation, frequency distribution analysis was performed on the APT results. The entire APT data set was divided into 200-atom bins, the composition of each bin was calculated and a histogram was plotted. For a random solid solution, a binomial frequency distribution is expected. Any deviation from randomness will lead to a deviation from binomial distribution. The frequency distribution analysis of Li, Ni, Mn and O in layered-LNMO is shown in Fig. 2a–d. Pearson coefficient test can be used to measure the statistical relevance of the observed deviation from randomness^{52–54}. Pearson coefficients tending towards 1 indicate statistically relevant extent of compositional segregation^{52,55}. The Pearson coefficients for elemental Li and Ni obtained from the 200-atom bin size frequency distribution analysis were 0.869 and 0.792, respectively; Mn and O had Pearson coefficient of 0.253 and 0.391, respectively. The NiO, MnO₃ and O₂ also had higher Pearson coefficient values of 0.535, 0.201 and 0.129, respectively, with all other molecular species below 0.1. Also all these elemental and molecular species with >0.1 Pearson

coefficients resulted in P values <0.001 at 95% confidence level during the null-hypothesis testing. These higher Pearson coefficient values and very low P values reaffirm the existence of statistically significant extent of compositional segregation in as-fabricated layered-LNMO.

Li, Ni, Mn and O distribution in Cycled layered-LNMO. On charge–discharge cycling of layered-LNMO cathodes with pre-existing Ni-rich regions, an additional Ni-rich surface reconstruction layer (SRL) has been found to form and grow as a function of cycling^{15–18}. By detailed STEM, EDS and EELS measurements, a compositional partitioning of Ni and Mn has been observed within the SRL. As the Li concentration is expected to vary between the SRL and bulk of the cathode nanoparticle as a function of cycling, layered-LNMO cathodes cycled for 45 cycles were examined by APT. Needle-shaped APT specimens were fabricated from four different cycled layered-LNMO particles and during the needle preparation the needle specimen apex was kept very close to the top surface of the particles. The overall composition for each of the APT results from the four cycled layered-LNMO particles and two as-fabricated layered-LNMO particles are given below in Table 1.

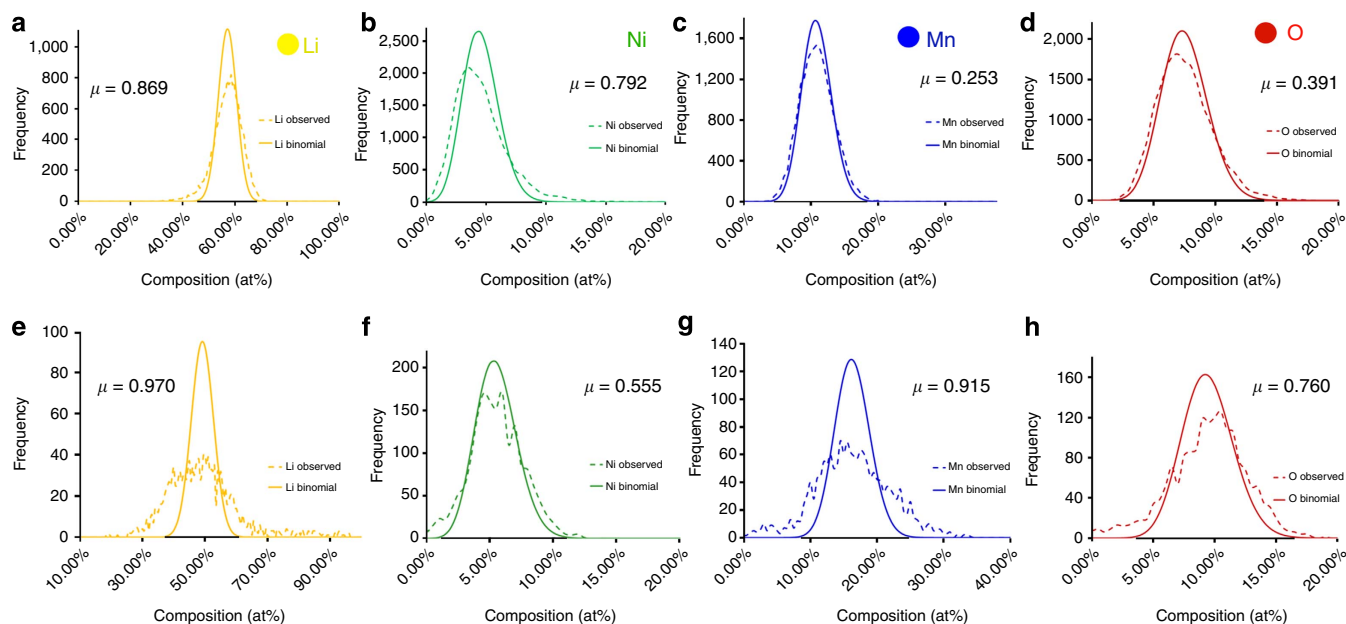


Figure 2 | Statistical analysis of element segregation in layered-LNMO. Frequency histogram of as-fabricated layered-LNMO (**a**) Li, (**b**) Ni, (**c**) Mn and (**d**) O with corresponding Pearson coefficients (μ) compared with frequency histogram of cycled layered-LNMO (**e**) Li, (**f**) Ni (**g**) Mn, (**h**) O indicating a high degree of non-uniformity in distribution of Li, Ni, Mn and O in both as-fabricated and cycled Li_{1.2}Ni_{0.2}Mn_{0.6}O₂.

Table 1 | Composition of as-fabricated and cycled layered-LNMO.

Material	Particle	Concentration (at %)			
		Li	O	Mn	Ni
As-fabricated layered-LNMO	P1	41.61	35.66	16.6	6.13
	P2	40.75	36.25	17.03	5.96
Cycled layered-LNMO after 45 cycles	P1	30.67	35.37	24.4	9.56
	P2	32.59	33.86	25.61	7.94
	P3	34.59	34.6	23.21	7.6
	P4	34.91	34.48	21.38	9.23

The quantified overall composition of 2 different nanoparticles of as-fabricated layered-LNMO and 4 different nanoparticles from cycled layered-LNMO after 45 cycles.

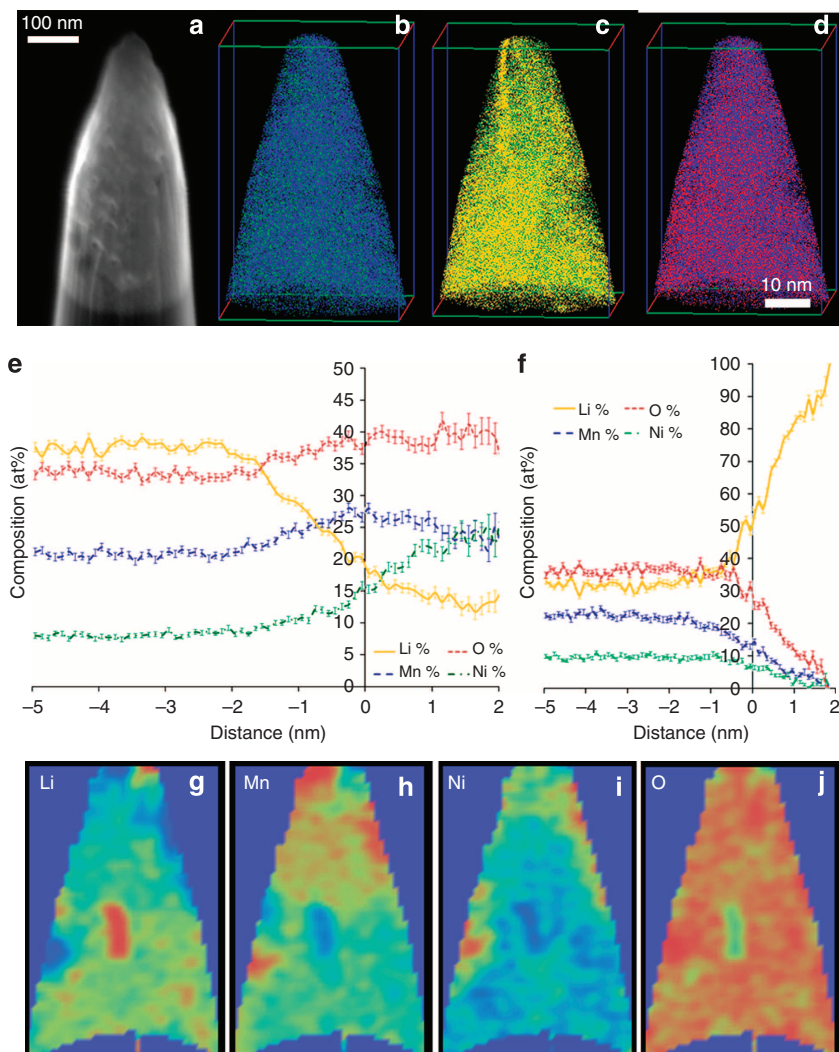


Figure 3 | APT results of cycled layered-LNMO. (a) The SEM image of the needle specimen of the cycled layered-LNMO (b–d) ion map of Mn and Ni, Ni and Li, Mn and O respectively. (e) Proximity histogram across a 14 at% Ni isocomposition surface and (f) proximity histogram across a Li-rich isocomposition surface. (g–j) 2D composition maps of Li, Mn, Ni and O for a 5-nm thick slice through a Li-rich inclusion.

A reduction in Li concentration and increase in the Mn and Ni concentration is observed in the cycled layered-LNMO specimens, in agreement with previous literature postulating a loss of Li as a function of cycling^{15,56}. Two-dimensional composition plots of Li, Ni, Mn and O, as shown in Fig. 3d–g, show that Li, Ni and Mn partially segregate. A proximity histogram plotted across a Ni 14 at% isocomposition surface, shown in Fig. 3e, illustrates the interface between the Ni-rich and Ni-depleted regions within the reconstruction. The proxygram highlights that Li is depleted where Ni is enriched, and that Mn is enriched at the interface between Ni- and Li-rich regions. A second proximity histogram across a Li-rich region indicates a very high Li concentration reaching nearly 100 at%. This apparently faceted region may correspond to a void formed inside the cathode nanoparticle during cycling, with an accumulation of Li. Comparison of the frequency histograms for Li, Mn, Ni and O in the cycled and as-fabricated layered-LNMO indicates an increased phase separation of Li, Mn and O (as indicated by the higher Pearson coefficient for Li, Mn and O of 0.970, 0.915, 0.76, respectively, shown in Fig. 2e–h). The Pearson coefficient of Ni was observed to be 0.555, indicating Ni enrichment near the surface of cycled cathode materials. It is to be noted that recent STEM imaging and EDS measurements observed similar Ni enrichment in as-

fabricated and cycled layered-LNMO particles. However, the pre-existing Ni-rich regions in the as-fabricated specimens were not captured within the APT reconstructions from the four cycled layered-LNMO particles. Pearson coefficient of molecular species of NiO (0.523), MnO (0.281), MnO₂ (0.259), MnO₃ (0.353), Ni₂O (0.331), O₂ (0.218) and NiO₃ (0.165) were also above 0.1. Each elemental and molecular species with a >0.1 Pearson coefficient values also showed a *P* value <0.001 at 95% confidence interval during null-hypothesis testing, establishing statistically significant segregation of these species in the cycled layered-LNMO.

Analysis of spinel-LNMO for technique validation. In contrast with layered-LNMO specimens, STEM-EDS mapping of spinel-LNMO indicates a uniform distribution of Mn, Ni and O, as shown in Fig. 4a–d. A mass-to-charge spectra from APT analysis of spinel-LNMO, provided in Supplementary Fig. 1, indicates a distribution of elemental and molecular ions similar to the as-fabricated layered-LNMO. Elemental ions of Li, Mn, Ni and O correspond to 74.23% of the ions detected; 24.2% of the ions detected correspond to O₂, MnO, NiO, MnO₂ and MnO₃ combined, and the remaining 1.58% includes all other complex molecular ions. APT reconstructions of the spinel-LNMO

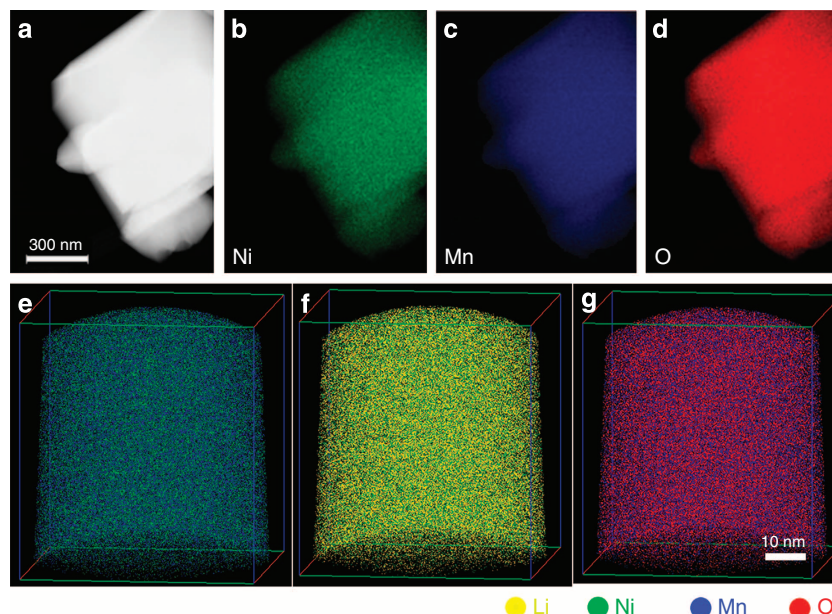


Figure 4 | Comparison of TEM EDS tomography with APT results of spinel-LNMO: TEM EDS mapping (a–d) and APT results (e–g) for $\text{LiNi}_{0.5}\text{Mn}_{1.5}\text{O}_4$ showing uniform distribution of all elements.

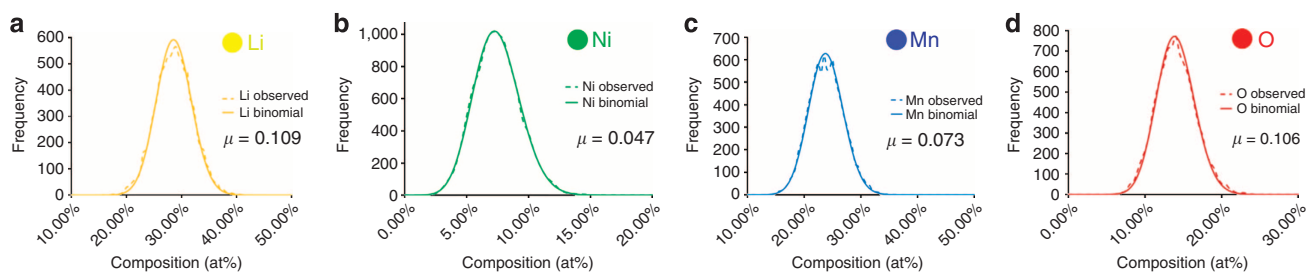


Figure 5 | Statistical analysis of element segregation in spinel-LNMO: Frequency distributions of Li, Ni, Mn and O in spinel-LNMO with corresponding Pearson coefficients (μ). (a–d) showing distributions rather close to uniform for Li, Ni, Mn, and O.

indicated uniform distributions of Li, Ni, Mn and O, as shown in Fig. 4e–g, in agreement with the STEM–EDS results for Ni, Mn and O. The APT-measured composition of spinel-LNMO was 20.06 ± 0.03 at % Li, 9.59 ± 0.02 at % Ni, 27.28 ± 0.03 at % Mn and 43.06 ± 0.04 at % O. The expected composition of these spinel-LNMO specimens is 14.29 at % Li, 7.14 at % Ni, 21.43 at % Mn and 57.14 at % O. As it is expected that oxygen will be underestimated with the 20-pJ laser energy, it is more sensible to renormalize the Li, Ni and Mn ratios excluding oxygen, for example, as $M/(\text{Li} + \text{Mn} + \text{Ni})$. Cation ratios estimated in this manner were 0.35 for Li, 0.48 for Mn, and 0.17 for Ni. The expected cation ratios for stoichiometric $\text{LiNi}_{0.5}\text{Mn}_{1.5}\text{O}_4$ are 0.33 for Li, 0.5 for Mn, and 0.17 for Ni, in excellent agreement with APT results, reinforcing the accuracy of APT in measuring Li, Ni and Mn in these samples.

Frequency distribution analysis of the APT results from spinel LNMO was conducted to quantify the uniformity of the distribution of each element. Figure 5a–d shows the observed frequency distributions of Li, Ni, Mn and O compared with a binomial distribution. It is clear that spinel-LNMO has a more uniform distribution compared to the as-fabricated layered-LNMO shown in Fig. 2. The Pearson coefficients estimated from the 200 atom bin size frequency distribution analysis for Li, Ni, Mn and O were 0.109, 0.047, 0.073 and 0.106 respectively (shown as inset in Fig. 5), all indicating a very close to uniform

distribution. The Pearson coefficient estimated for all the molecular species were also well below 0.1. A Pearson coefficient value close to 0 is indicative of a uniform distribution of elements^{52,55}. The P values estimated at a 95% confidence interval for Li and O was observed to be below 0.001 and the P value for Mn and Ni were 0.095 and 0.568. These P values in combination with the Pearson coefficient values when compared with layered-LNMO results indicate that there is only a minor deviation from random distribution for Li and O, but Ni and Mn are distributed rather uniformly in the spinel-LNMO APT result.

Discussion

The Li segregation to Mn-rich, Ni-depleted regions in as-fabricated layered-LNMO suggests a Li_2MnO_3 phase with only minor Ni. The Ni-enriched regions with lower Li concentration can be attributed to a $\text{Li}(\text{Ni}_{0.5}\text{Mn}_{0.5})\text{O}_2$ phase. These APT results are consistent with STEM–EDS results from the same materials¹¹. The APT results consistent with $\text{Li}_{1.2}\text{Ni}_{0.2}\text{Mn}_{0.6}\text{O}_2$ being a nanoscale composite mixture of LiMO_2 (R-3m) with Li_2MO_3 (C2/m) having varying amounts of Li, Mn, and Ni in each of these phases. Partitioning of Li, Ni, and Mn can lead to variation of local electrochemical properties. Recently, it was demonstrated that the capacity fading in layered-LNMO is closely related to the Ni distribution⁵⁷, but those results lacked information about

the Li distribution. It is plausible that the local depletion of Li leads to partial deactivation of a particle with cycling, which may contribute to the capacity and voltage fading. APT results from the cycled LNMO provide evidence for Li loss. Partial segregation of Li, Mn and Ni to different regions in the cycled layered-LNMO is shown along with an increased extent of phase separation of Li, Mn and O.

Prior high spatial resolution studies of Li-ion cathode materials have similarly been left to infer the behaviour of Li by studying the changes in the local crystallography and the transition metal cation concentration. This study conclusively demonstrates that laser-assisted APT can be used to not only quantify the Ni and Mn composition in 3D but also the Li, and with sufficient accuracy to postulate the phase. There do not appear to be any barriers to studying the spatial distribution of Li for different synthesis methods, common cathode materials and for varying extents of electrochemical cycling of the cathode material. Quantifying the Li distribution by APT can impact the optimization of cathode synthesis procedures to achieve the highest performance, provide key insights toward the atomic-scale mechanism of capacity decay as a function of cycling, and aid in the effort to create novel Li-ion materials with prolonged lifetimes.

In summary, by comparing the as-fabricated and cycled layered-LNMO we have demonstrated a cycling-induced increased segregation of Li, Mn and O. The APT results of cycled layered-LNMO represent one of the first instances of direct evidence for Li loss in cycled cathode materials, consistent with previous TEM studies and typical explanations for irreversible capacity loss upon cycling of layered cathode materials. Comparison with compositionally uniform spinel-LNMO unambiguously establishes that the laser-assisted APT can differentiate Li segregation in battery-relevant materials at sub-nanometre-scale, in 3D. We anticipate significant application of APT analysis for understanding elemental distribution not just in the as-fabricated cathode materials, but also in electrochemically cycled materials to obtain important insight towards understanding capacity degradation in the cathode materials as a function of extent of cycling.

Methods

Material synthesis. $\text{Li}_{1.2}\text{Ni}_{0.2}\text{Mn}_{0.6}\text{O}_2$ was synthesized by wet chemical process as described briefly here. Nickel sulfate hexahydrate ($\text{NiSO}_4 \cdot 6\text{H}_2\text{O}$), manganese sulfate monohydrate ($\text{MnSO}_4 \cdot \text{H}_2\text{O}$), sodium hydroxide (NaOH), and ammonium hydroxide ($\text{NH}_3 \cdot \text{H}_2\text{O}$) were used as the starting materials to prepare $\text{Ni}_{0.25}\text{Mn}_{0.75}(\text{OH})_2$ precursor. The precursor material was washed with hot water to remove residual sodium and sulfuric species, then filtered and dried inside a vacuum oven set at 80°C for 24 h. $\text{Ni}_{0.25}\text{Mn}_{0.75}(\text{OH})_2$ was mixed well with Li_2CO_3 and then calcined at 900°C for 15 h to form the cathode materials. Detailed experimental set-up for the synthesis of the materials was reported in Wang *et al.*⁵⁸ A facile solid-state reaction method, which is easy to scale up for mass production, was adopted to synthesize the spinel $\text{LiNi}_{0.5}\text{Mn}_{1.5}\text{O}_4$. In detail, $\text{LiNi}_{0.5}\text{Mn}_{1.5}\text{O}_4$ was prepared by ball milling a mixture of Li_2CO_3 , NiO and MnCO_3 (all from Aldrich) in stoichiometric amount for 4 h followed by calcination at 900°C for 24 h in air with the heating rate of $10^\circ\text{C min}^{-1}$ and cooling rate of 5°C min^{-1} .

Electrochemical cycling. The electrochemical cycling of layered-LNMO particles were conducted using coin cells configuration with metallic Li as counter electrode, separator of Celgard K1640 monolayer polyethylene membrane, with 1:2 volume ratio, 1 M Lithium hexafluorophosphate (LiPF₆) dissolved in ethyl carbonate and Dimethyl carbonate (DMC) electrolyte in an argon-filled MBraun glovebox. The 45-cycle sample studied in this work was cycled at a rate of 0.1 C between 2.0–4.7 V versus Li/Li^+ at room temperature. The first cycle charge/discharge profile and ‘charge and discharge’ capacities as function of cycle numbers at 2.0–4.7 V versus Li/Li^+ are given in Supplementary Fig. 2. The cycled coin cells were disassembled and the cycled electrode was immersed in DMC for 12 h followed by washing by DMC for three times. The washed electrodes were dried in vacuum for 12 h. The cathode material was removed from the Al-foil and grounded to fine powders and deposited on a lacey carbon TEM grid for TEM imaging. The nanoparticles for APT specimens were lifted out from the TEM grid using lift-out method described below.

STEM/EDS mapping. The STEM and EDS mapping was performed using an FEI Tecnai Osiris microscope at 200 kV. The samples were dispersed onto a holey-carbon TEM grid and imaged accordingly. The FEI Tecnai Osiris microscope is equipped with a state-of-the-art Super-X EDS detector system, which allows efficient and fast mapping at nanoscale.

Atom probe specimen preparation. Needle-shaped specimens for APT analysis were prepared by lift-out procedure using an FEI Helios 600 Nanolab focused-ion-beam/scanning electron microscope (FIB/SEM). $\text{Li}_{1.2}\text{Ni}_{0.2}\text{Mn}_{0.6}\text{O}_2$ nanoparticles were dispersed on a Si substrate; individual nanoparticles were lifted out by contact with OmniProbe nanomanipulator and transferred onto a Si microtip array. Once the nanoparticles were placed on top of Si microtips, electron-beam-assisted Pt deposition was used to coat the individual nanoparticles. All manipulation of nanoparticles and Pt deposition were done using only the electron beam without Ga-ion beam imaging. After Pt deposition, the nanoparticles were subjected to annular milling using Ga-ion beam to form the final needle specimens of the nanoparticles attached to the Si microtip array. If cavities were observed between a nanoparticle and the Si microtip, electron-beam-assisted Pt deposition was also performed during annular milling. Initial annular milling was conducted at 30 kV and final milling was performed using 2 kV to minimize Ga contamination in the final needle specimen. A schematic of the specimen preparation method is given in Supplementary Fig. 3.

Atom probe tomography. Laser-assisted APT analysis was conducted using a CAMECA LEAP4000 × HR atom probe tomography system with a 355-nm ultraviolet laser, 20-pJ laser pulse energy, 40 K specimen temperature and evaporation rate maintained at 0.005 atoms per pulse. APT data were reconstructed and analysed using IVAS 3.6.6 software.

References

- Tarascon, J. M. & Armand, M. Issues and challenges facing rechargeable lithium batteries. *Nature* **414**, 359–367 (2001).
- Croy, J. R., Abouimrane, A. & Zhang, Z. Next-generation lithium-ion batteries: The promise of near-term advancements. *MRS Bull.* **39**, 407–415 (2014).
- Etacheri, V., Marom, R., Elazari, R., Salitra, G. & Aurbach, D. Challenges in the development of advanced Li-ion batteries: a review. *Energy Environ. Sci.* **4**, 3243–3262 (2011).
- Goodenough, J. B. & Kim, Y. Challenges for rechargeable Li batteries. *Chem. Mater.* **22**, 587–603 (2010).
- Ellis, B. L., Lee, K. T. & Nazar, L. F. Positive electrode materials for Li-ion and Li-batteries. *Chem. Mater.* **22**, 691–714 (2010).
- Thackeray, M. M., Johnson, C. S., Vaughey, J. T., Li, N. & Hackney, S. A. Advances in manganese-oxide ‘composite’ electrodes for lithium-ion batteries. *J. Mater. Chem.* **15**, 2257–2267 (2005).
- Armstrong, A. R. *et al.* Demonstrating oxygen loss and associated structural reorganization in the lithium battery cathode $\text{Li}[\text{Ni}_{0.2}\text{Li}_{0.2}\text{Mn}_{0.6}]\text{O}_2$. *J. Am. Chem. Soc.* **128**, 8694–8698 (2006).
- Kim, J. S., Johnson, C. S., Vaughey, J. T., Thackeray, M. M. & Hackney, S. A. Electrochemical and structural properties of $\text{xLi}(2)\text{M}'\text{O}-3$ center dot $(1-x)\text{LiMn}_{0.5}\text{Ni}_{0.5}\text{O}_2$ electrodes for lithium batteries ($\text{M}' = \text{Ti, Mn, Zr}$; $0 < x < 0.3$). *Chem. Mater.* **16**, 1996–2006 (2004).
- Thackeray, M. M., Kang, S. H., Johnson, C. S., Vaughey, J. T., Benedek, R. & Hackney, S. A. Li_2MnO_3 -stabilized LiMO_2 ($\text{M} = \text{Mn, Ni, Co}$) electrodes for lithium-ion batteries. *J. Mater. Chem.* **17**, 3112–3125 (2007).
- Genc, A. *et al.* XEDS STEM tomography for 3D chemical characterization of nanoscale particles. *Ultramicroscopy* **131**, 24–32 (2013).
- Gu, M. *et al.* Conflicting roles of nickel in controlling cathode performance in lithium ion batteries. *Nano Lett.* **12**, 5186–5191 (2012).
- Gu, M. *et al.* Nanoscale phase separation, cation ordering, and surface chemistry in pristine $\text{Li}_{1.2}\text{Ni}_{0.2}\text{Mn}_{0.6}\text{O}_2$ for Li-ion batteries. *Chem. Mater.* **25**, 2319–2326 (2013).
- Hong, J., Seo, D. H., Kim, S. W., Gwon, H., Oh, S. T. & Kang, K. Structural evolution of layered $\text{Li}_{1.2}\text{Ni}_{0.2}\text{Mn}_{0.6}\text{O}_2$ upon electrochemical cycling in a Li rechargeable battery. *J. Mater. Chem.* **20**, 10179–10186 (2010).
- Lei, C. H., Barenjo, J., Wen, J. G., Petrov, I., Kang, S. H. & Abraham, D. P. Local structure and composition studies of $\text{Li}_{1.2}\text{Ni}_{0.2}\text{Mn}_{0.6}\text{O}_2$ by analytical electron microscopy. *J. Power Sources* **178**, 422–433 (2008).
- Yan, P. *et al.* Evolution of lattice structure and chemical composition of the surface reconstruction layer in $\text{Li}_{1.2}\text{Ni}_{0.2}\text{Mn}_{0.6}\text{O}_2$ cathode material for lithium ion batteries. *Nano Lett.* **15**, 514–522 (2015).
- Lin, F. *et al.* Surface reconstruction and chemical evolution of stoichiometric layered cathode materials for lithium-ion batteries. *Nat. Commun.* **5**, 3529 (2014).
- Boulineau, A., Simonin, L., Colin, J. F., Bourbon, C. & Patoux, S. First evidence of manganese-nickel segregation and densification upon cycling in Li-Rich layered oxides for lithium batteries. *Nano Lett.* **13**, 3857–3863 (2013).
- Xu, B., Fell, C. R., Chi, M. F. & Meng, Y. S. Identifying surface structural changes in layered Li-excess nickel manganese oxides in high voltage lithium

- ion batteries: A joint experimental and theoretical study. *Energy Environ. Sci.* **4**, 2223–2233 (2011).
19. Gu, M. *et al.* Formation of the spinel phase in the layered composite cathode used in Li-ion batteries. *ACS Nano* **7**, 760–767 (2013).
 20. Xiao, J. *et al.* High-performance LiNi_{0.5}Mn_{1.5}O₄ Spinel controlled by Mn³⁺ concentration and site disorder. *Adv. Mater.* **24**, 2109–2116 (2012).
 21. Hassoun, J., Panero, S., Reale, P. & Scrosati, B. A new, safe, high-rate and high-energy polymer lithium-ion battery. *Adv. Mater.* **21**, 4807–4810 (2009).
 22. Kunduraci, M., Al-Sharab, J. F. & Amatucci, G. G. High-power nanostructured LiMn_{2-x}Ni_xO₄ high-voltage lithium-ion battery electrode materials: Electrochemical impact of electronic conductivity and morphology. *Chem. Mater.* **18**, 3585–3592 (2006).
 23. Lee, E. & Persson, K. A. Revealing the coupled cation interactions behind the electrochemical profile of Li_xNi_{0.5}Mn_{1.5}O₄. *Energy Environ. Sci.* **5**, 6047–6051 (2012).
 24. Kim, J. H., Myung, S. T., Yoon, C. S., Kang, S. G. & Sun, Y. K. Comparative study of LiNi_{0.5}Mn_{1.5}O₄-delta and LiNi_{0.5}Mn_{1.5}O₄ cathodes having two crystallographic structures: Fd(3)over-bar and P4(3)32. *Chem. Mater.* **16**, 906–914 (2004).
 25. Wang, L. P., Li, H., Huang, X. J. & Baudrin, E. A comparative study of Fd-3m and P4(3)32 'LiNi_{0.5}Mn_{1.5}O₄'. *Solid State Ionics* **193**, 32–38 (2011).
 26. Patoux, S. *et al.* High voltage nickel manganese spinel oxides for Li-ion batteries. *Electrochim. Acta* **53**, 4137–4145 (2008).
 27. Zheng, J. M. *et al.* Enhanced Li⁺ ion transport in LiNi_{0.5}Mn_{1.5}O₄ through control of site disorder. *Phys. Chem. Chem. Phys.* **14**, 13515–13521 (2012).
 28. Wang, F. *et al.* Tracking lithium transport and electrochemical reactions in nanoparticles. *Nat. Commun.* **3**, 1–8 (2012).
 29. Shao-Horn, Y., Croguennec, L., Delmas, C., Nelson, E. C. & O'Keefe, M. A. Atomic resolution of lithium ions in LiCoO₂. *Nat. Mater.* **2**, 464–467 (2003).
 30. Chung, S. Y., Choi, S. Y., Yamamoto, T. & Ikuhara, Y. Atomic-scale visualization of antisite defects in LiFePO₄. *Phys. Rev. Lett.* **100**, 125502 (2008).
 31. Oshima, Y. *et al.* Direct imaging of lithium atoms in LiV₂O₄ by spherical aberration-corrected electron microscopy. *J. Electron. Microscop.* **59**, 457–461 (2010).
 32. Liu, X. S. *et al.* Distinct charge dynamics in battery electrodes revealed by in situ and operando soft X-ray spectroscopy. *Nat. Commun.* **4**, 1–8 (2013).
 33. Devaraj, A., Colby, R., Hess, W. P., Perea, D. E. & Thevuthasan, S. Role of photoexcitation and field ionization in the measurement of accurate oxide stoichiometry by laser-assisted atom probe tomography. *J. Phys. Chem. Lett.* **4**, 993–998 (2013).
 34. Kelly, T. F. & Larson, D. J. The second revolution in atom probe tomography. *MRS Bull.* **37**, 150–158 (2012).
 35. Kelly, T. F. & Miller, M. K. Invited review article: atom probe tomography. *Rev. Sci. Instrum.* **78** (2007).
 36. Kelly, T. F. *et al.* Atom probe tomography of electronic materials. *Annu. Rev. Mater. Res.* **37**, 681–727 (2007).
 37. Vilayuganapathy, S. *et al.* Subsurface synthesis and characterization of Ag nanoparticles embedded in MgO. *Nanotechnology* **24**, 1–8 (2013).
 38. Devaraj, A., Colby, R., Vurpillot, F. & Thevuthasan, S. Understanding atom probe tomography of oxide-supported metal nanoparticles by correlation with atomic-resolution electron microscopy and field evaporation simulation. *J. Phys. Chem. Lett.* **5**, 1361–1367 (2014).
 39. Greiwe, G. H., Balogh, Z. & Schmitz, G. Atom probe tomography of lithium-doped network glasses. *Ultramicroscopy* **141**, 51–55 (2014).
 40. Heard, D. W., Boselli, J., Rioja, R., Marquis, E. A., Gauvin, R. & Brochu, M. Interfacial morphology development and solute trapping behavior during rapid solidification of an Al-Li-Cu alloy. *Acta Mater.* **61**, 1571–1580 (2013).
 41. Krug, M. E., Seidman, D. N. & Dunand, D. C. Creep properties and precipitate evolution in Al-Li alloys microalloyed with Sc and Yb. *Mat. Sci. Eng. A-Struct.* **550**, 300–311 (2012).
 42. Gault, B. *et al.* Atom probe microscopy investigation of Mg site occupancy within delta' precipitates in an Al-Mg-Li alloy. *Scripta Mater.* **66**, 903–906 (2012).
 43. Deschamps, A., Sigli, C., Mourey, T., de Geuser, F., Lefebvre, W. & Davo, B. Experimental and modelling assessment of precipitation kinetics in an Al-Li-Mg alloy. *Acta Mater.* **60**, 1917–1928 (2012).
 44. Gault, B., de Geuser, F., Bourgeois, L., Gable, B. M., Ringer, S. P. & Muddle, B. C. Atom probe tomography and transmission electron microscopy characterisation of precipitation in an Al-Cu-Li-Mg-Ag alloy. *Ultramicroscopy* **111**, 683–689 (2011).
 45. Monachon, C., Krug, M. E., Seidman, D. N. & Dunand, D. C. Chemistry and structure of core/double-shell nanoscale precipitates in Al-6.5Li-0.07Sc-0.02Yb (at.%). *Acta Mater.* **59**, 3398–3409 (2011).
 46. Krug, M. E., Dunand, D. C. & Seidman, D. N. Effects of Li additions on precipitation-strengthened Al-Sc and Al-Sc-Yb alloys. *Acta Mater.* **59**, 1700–1715 (2011).
 47. Xiong, X. Y., Moutsos, S., King, R. & Muddle, B. Quantitative analysis of precipitate compositions in an Al-Li-Mg-Cu alloy using atom probe tomography. *Mater. Sci. Forum* **654-656**, 914–917 (2010).
 48. Krug, M. E., Dunand, D. C. & Seidman, D. N. Composition profiles within Al(3)Li and Al(3)Sc/Al(3)Li nanoscale precipitates in aluminum. *Appl. Phys. Lett.* **92**, 124107 (2008).
 49. Santhanagopalan, D. *et al.* Effects of laser energy and wavelength on the analysis of LiFePO₄ using laser assisted atom probe tomography. *Ultramicroscopy* **148**, 57–66 (2015).
 50. Diercks, D. R. *et al.* Evidence for anisotropic mechanical behavior and nanoscale chemical heterogeneity in cycled LiCoO₂. *J. Electrochem. Soc.* **161**, F3039–F3045 (2014).
 51. Hellman, O. C., Vandenbroucke, J. A., Rusing, J., Isheim, D. & Seidman, D. N. Analysis of three-dimensional atom-probe data by the proximity histogram. *Microsc. Microanal.* **6**, 437–444 (2000).
 52. Gault, B., Moody, M. P., Cairney, J. M. & Ringer, S. P. *Atom Probe Microscopy* (Springer, 2012).
 53. Moody, M. P., Stephenson, L. T., Ceguerra, A. V. & Ringer, S. P. Quantitative binomial distribution analyses of nanoscale like-solute atom clustering and segregation in atom probe tomography data. *Microsc. Res. Techniq.* **71**, 542–550 (2008).
 54. Moody, M. P., Stephenson, L. T., Liddicoat, P. V. & Ringer, S. P. Contingency table techniques for three dimensional atom probe tomography. *Microsc. Res. Techniq.* **70**, 258–268 (2007).
 55. Devaraj, A. *et al.* Nanoscale phase separation in epitaxial Cr-Mo and Cr-V alloy thin films studied using atom probe tomography: Comparison of experiments and simulation. *J. Appl. Phys.* **116**, 193512 (2014).
 56. Yan, P. *et al.* Probing the degradation mechanism of Li₂MnO₃ cathode for Li-ion batteries. *Chem. Mater.* **27**, 975–982 (2015).
 57. Zheng, J. *et al.* Mitigating voltage fade in cathode materials by improving the atomic level uniformity of elemental distribution. *Nano Lett.* **14**, 2628–2635 (2014).
 58. Wang, D. P., Belharouak, I., Koenig, G. M., Zhou, G. W. & Amine, K. Growth mechanism of Ni_{0.3}Mn_{0.7}CO₃ precursor for high capacity Li-ion battery cathodes. *J. Mater. Chem.* **21**, 9290–9295 (2011).

Acknowledgements

The funding for the research described in this paper was from a Laboratory Directed Research and Development fund from the Chemical Imaging Initiative at Pacific Northwest National Laboratory (PNNL). PNNL is a multiprogram national laboratory operated by Battelle Memorial Institute, under Contract No. DE-AC05-76RLO1830 for the U.S. Department of Energy (DOE). RC would like to thank the Wiley Postdoctoral Fellowship for research funding. All the characterization was conducted in the William R. Wiley Environmental Molecular Sciences Laboratory (EMSL), a national scientific user facility sponsored by DOE's Office of Biological and Environmental Research and located at PNNL.

Author contributions

A.D., R.C. and S.T. conceived the research and A.D. executed the APT specimen preparation, APT experiments and analysed the results. M.G., P.Y., C.M.W. and A.G. conducted the STEM-EDS mapping. J.M.Z., J.X., J.G.Z., I.B., D.W. and K.A. synthesized the cathode materials and conducted the electrochemical cycling. A.D. and R.C. wrote the manuscript with input from all the other authors.

Additional information

Supplementary Information accompanies this paper at <http://www.nature.com/naturecommunications>

Competing financial interests: The authors declare no competing financial interests.

Reprints and permission information is available online at <http://npng.nature.com/reprintsandpermissions/>

How to cite this article: Devaraj, A. *et al.* Visualizing nanoscale 3D compositional fluctuation of lithium in advanced lithium-ion battery cathodes. *Nat. Commun.* **6**:8014 doi: 10.1038/ncomms9014 (2015).



This work is licensed under a Creative Commons Attribution 4.0 International License. The images or other third party material in this article are included in the article's Creative Commons license, unless indicated otherwise in the credit line; if the material is not included under the Creative Commons license, users will need to obtain permission from the license holder to reproduce the material. To view a copy of this license, visit <http://creativecommons.org/licenses/by/4.0/>